Influence of GaAs(001) substrate misorientation towards {111} on the optical properties of $In_xGa_{1-x}As/GaAs$

D. H. Rich, K. Rammohan, Y. Tang, and H. T. Lin
Photonic Materials and Devices Laboratory, Department of Materials Science and Engineering, University of Southern California, Los Angeles, California 90089-0241

R. S. Goldman, H. H. Wieder, and K. L. Kavanagh
Department of Electrical and Computer Engineering, University of California, San Diego, La Jolla, California 92093-0407

(Received 10 January 1995; accepted 1 April 1995)

Local variations in the optical properties of thick $In_{0.13}Ga_{0.87}As$ films grown on GaAs(001) substrates misoriented toward {111} planes have been studied with polarized and spectrally-resolved cathodoluminescence (CL) imaging. The degree of anisotropic relaxation and density of dark line defects (DLDs) in CL was found to depend on the choice of the substrate miscut orientation. An enhanced anisotropy in DLD density and strain relaxation was found for a misorientation towards (111)*A* relative to that for a misorientation towards (111)*B*. Local variations and spatial correlations in polarization anisotropy, band-gap energy shifts, luminescence efficiency, and defect-induced long-wavelength luminescence were examined. © *1995 American Vacuum Society.*

I. INTRODUCTION

Owing to the importance of attaining high-quality epitaxial growth of strained $In_xGa_{1-x}As$ grown on GaAs for applications in high electron mobility transistors, lasers, detectors, and light modulators, it is necessary to examine factors pertaining to the starting GaAs substrate that influence the resulting structural, optical, and electronic properties of the $In_xGa_{1-x}As$ film. One such factor is the misorientation of the GaAs substrate. The influence of substrate misorientation is found to affect the magnitude of asymmetry in the formation of ⟨110⟩-oriented 60° misfit dislocations in $In_xGa_{1-x}As/GaAs$ during strain relaxation.[1–3] Even on a nonvicinal (no misorientation) substrate, the chemical inequivalence of orthogonal α and β dislocations induces a preferred relaxation direction during growth of $In_xGa_{1-x}As$ on GaAs(001).[4,5] Due to an asymmetry in strain relaxation, a polarization anisotropy in excitonic luminescence is expected to occur. Local polarization anisotropies have recently been measured in step-graded $In_xGa_{1-x}As$ and single thin $In_{0.06}Ga_{0.94}As$ films.[3,6] In these studies, local variations in strain relaxation due to inhomogeneities in defect density have been observed, giving rise to measured μm-scale variations in polarization of excitonic emission that correlate with dark line defect (DLD) positions and orientation.[1,3,6] It is therefore reasonable to study the feasibility of tailoring the optical polarization properties of the $In_xGa_{1-x}As/GaAs$ system for future photonic applications by choosing suitable substrate misorientations.

In this article, we examine the influence of the substrate misorientation towards {111} planes on the local optical properties using spectrally and spatially resolved cathodoluminescence (CL). We have utilized a new variation in the CL imaging technique, in which a combination of linearly polarized CL (LPCL)[7,8] and CL wavelength imaging (CLWI)[9] is used to study strain-induced local changes in the band gap and polarization of excitonic luminescence. The LPCL and CLWI approaches have recently been used to assess strain relaxation in thin films of $In_{0.06}Ga_{0.94}As$ and step-graded $In_xGa_{1-x}As$.[1,3,6] The LPCL approach has also enabled a mapping of the spatial distribution of the stress tensor in thick films ($\gtrsim 1$ μm) of GaAs grown on Si by studying the excitonic transitions associated with the strain-split heavy-hole (hh) and light-hole (lh) bands of GaAs.[7,8] Polarization selection rules involving hh and lh excitonic luminescence in direct band-gap semiconductors depend on the form of the stress tensor.[10] We utilize CLWI to image the defect-, strain-, and composition-induced band-gap changes on the scale of ~ 1 μm, as the resolution is limited by the minority carrier diffusion. The presence of dislocations can induce additional nonradiative and radiative recombination channels, which can show up as long wavelength (less than the InGaAs band-gap excitonic energies).[11–13] A study of the spatial correlation of defect-induced radiative transitions with the DLDs associated with a decrease in band-gap excitonic emission may add further insights towards the understanding of strain relaxation.

II. EXPERIMENTAL DETAILS

Samples were grown by solid source molecular beam epitaxy. Details of the preparation and structural characterization techniques have been described elsewhere.[1] They consisted of 300 nm Si doped $In_{0.13}Ga_{0.87}As$ on 500 nm undoped GaAs buffers grown simultaneously on semi-insulating (001)-oriented GaAs substrates misoriented $2° \pm 0.05°$ towards (111)*A* and (111)*B* planes, each terminated with single Ga and As bonds, respectively.

X-ray rocking curve (XRC) measurements showed that the sample grown on the (111)*A*-misoriented substrate relaxed 96% and 41% in the [110] and [1$\bar{1}$0] directions, respectively, and the sample grown on the (111)*B*-misoriented substrates relaxed 72% and 84% in the [110] and [1$\bar{1}$0] directions, respectively. Thus, the relaxation anisotropy is substantially greater for the (111)*A* misorientation, while the total average relaxation for the (111)*B* misorientation (78%)

is greater than that for the (111)*A* misorientation (68.5%). For 60° misfit dislocations, an average strain relaxation of 0.02% occurs for a linear dislocation density of 1×10^4 cm^{-1}.[4] Assuming only 60° dislocations, the (111)*A* and (111)*B*-misoriented samples will have α misfit dislocation densities of 4.4 and 3.3 and β dislocation densities of 1.9 and 3.8 (in units of 10^5 cm^{-1}), respectively. These densities are substantially greater than the upper limit of $\sim 1 \times 10^4$ cm^{-1} required for being able to image individual misfit dislocations with CL, owing to the carrier diffusion length of ~ 1 μm. We therefore expect that in CL images showing DLDs, the DLD will be composed of bunches of misfit dislocations, as previously observed in other studies.[5,11]

Scanning monochromatic CL, CLWI and LPCL were performed with a modified JEOL 840-A scanning electron microscope. A rotatable linear polarizer was mounted *in vacuo* to perform polarization measurements.[7,8] The light collected was dispersed by a 0.25 m monochromator and detected with a liquid nitrogen cooled Ge *p-i-n* detector. An electron beam with a 15 keV beam energy and beam currents ranging from 1 to 50 nA were used to probe the samples which were cooled to 87 K.

In CLWI imaging the wavelength, λ_m, at which the intensity of luminescence is a maximum is mapped as a function of the spatial (x,y) position, and a gray-scale or false-color image representing these wavelengths is generated.[9] A scanning area of 128 μm$\times$94 μm in this study is discretized into 640$\times$480 pixels. In order to determine $\lambda_m(x,y)$, a spectrum consisting of 34 wavelength points (obtained from 34 discrete monochromatic CL images), varying from 918 to 934 nm, was obtained at each pixel position, thus enabling a mapping of the $In_xGa_{1-x}As$ band gap. Spectrally integrated CL images (panchromatic in the 918 to 934 nm range) were likewise obtained by summing the 34 discrete monochromatic images at each (x,y) pixel position.

LPCL spectra of the $In_xGa_{1-x}As$ excitonic luminescence were taken with the polarizer rotated to detect emission of light with $\mathbf{E}\perp[110]$ or $\mathbf{E}\|[110]$, where $\mathbf{E}$ is the electric field of the detected light. Likewise, monochromatic LPCL images were taken with the polarizer in these orientations. In order to emphasize the polarization variations, the ratio of these images at each (x,y) position are represented as $\log[I_\|(x,y)/I_\perp(x,y)]$, where $I_\perp$ and $I_\|$ are the pixel intensities under $\mathbf{E}\perp[110]$ and $\mathbf{E}\|[110]$ detection orientations, normalized to a 256-level gray scale. The $\perp$ and $\|$ subscripts are defined with respect to [110] in this study.

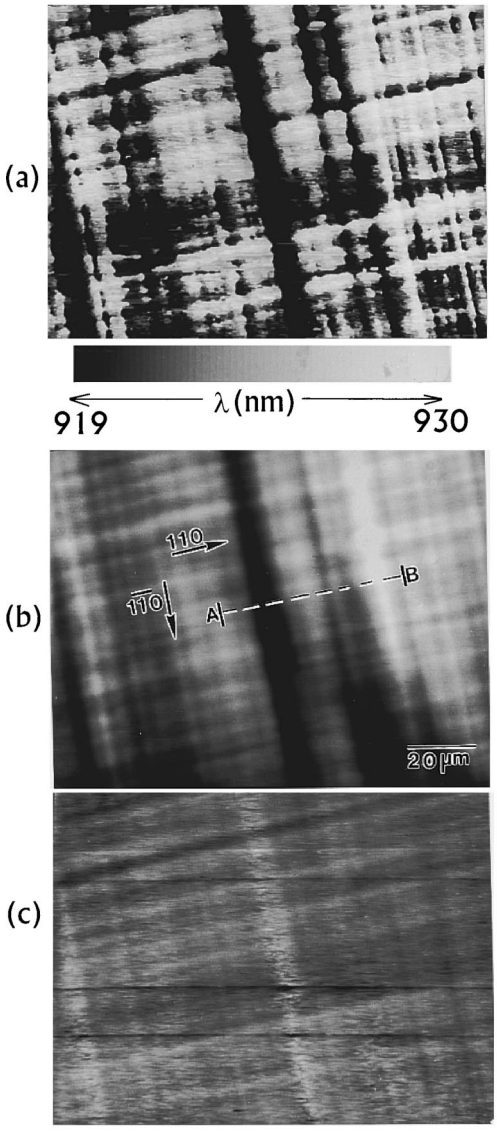

FIG. 1. CLWI, integrated CL intensity, and LPCL images in (a), (b), and (c), respectively, for the $In_{0.13}Ga_{0.87}As$ film grown on the (001) substrate misoriented 2° toward (111)*A*. A scale showing the mapping of wavelengths of peak CL intensity is shown in (a). The LPCL image in (c) is displayed as a 256-gray scale of $\log[I_\|(x,y)/I_\perp(x,y)]$ at $\lambda=929$ nm.

III. RESULTS AND DISCUSSION

A. Cathodoluminescence wavelength imaging

Figures 1(a) and 2(a) show CLWI images for the $In_{0.13}Ga_{0.87}As$ films grown on the GaAs(001) substrates misoriented towards (111)*A* and (111)*B*, respectively. The mapping of λ_m into a gray-scale representation is shown by the gray-bar key indicating the wavelength scale. Figures 1(b) and 2(b) show spectrally integrated CL intensity micrographs. Long streaks of a constant gray shade can be seen in Figs. 1(a) and 2(a) which correlate in position and orientation with the DLDs in the integrated CL intensity images. These DLDs have been observed previously in CL imaging of partially relaxed InGaAs films grown on GaAs.[5,11] The reduction in the luminescence efficiency is due to the presence of nonradiative recombination centers, likely caused by the presence of misfit dislocation cores and point defects left in the wake of dislocation propagation.[11] The spectrally-integrated images of Figs. 1(b) and 2(b) represent a spatial mapping of the excitonic luminescence efficiency, which is lowest in the regions of the DLDs. An asymmetry in DLD density is observed in the image of Fig. 1(b), with large dark bands oriented along the [110] direction. A stack plot of local spectra along an arbitrary [110]-oriented line [indicated by a dashed line and showing end points labeled *A* and *B* in Fig. 1(b)] is shown in Fig. 3. The distance Δx along this line where the electron beam was fixed is indicated. It is apparent that the peak position of the CL spectra varies with Δx. This

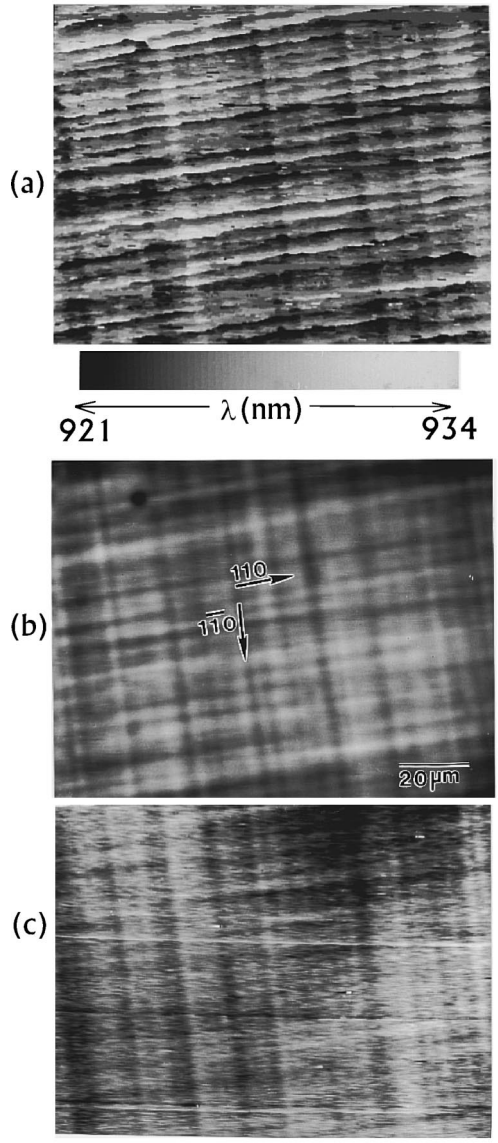

FIG. 2. CLWI, integrated CL intensity, and LPCL images in (a), (b), and (c), respectively, for the $In_{0.13}Ga_{0.87}As$ film grown on the (001) substrate misoriented 2° toward (111)*B*. A scale showing the mapping of wavelengths of peak CL intensity is shown in (a). The LPCL image in (c) is displayed as a 256-gray scale of $\log[I_{\parallel}(x,y)/I_{\perp}(x,y)]$ at $\lambda = 929$ nm.

local variation supplied the motivation for performing CLWI, which maps the peak intensity position of the CL spectra, λ_m, as a function of (x,y) position. In the CLWI image of Fig. 1(a), the regions corresponding to the dark lines appear as blue-shifted (towards shorter wavelengths) long bands along [110]. This relative blue-shift is indicative of a higher-compressive biaxial stress relative to red-shifted bands which run predominantly along [110]. The asymmetry is reversed in the CLWI image of Fig. 2(a) for the (111)*B* misorientation, where the principal DLD and CLWI banding direction is along [110]. Thus, the CLWI asymmetry is clearly linked to the choice of substrate misorientation.

B. Linearly polarized cathodoluminescence

In order to further understand the nature of the relaxation, we have performed LPCL imaging and spectroscopy over these same regions. Figures 1(c) and 2(c) show monochromatic LPCL images of $\log[I_{\parallel}(x,y)/I_{\perp}(x,y)]$ at $\lambda = 929$ nm. A series of local LPCL spectra corresponding to each of the unpolarized local spectra are shown in Fig. 3. The spectra were taken under the two polarization orientations, with $\mathbf{E}\perp$ [110] or $\mathbf{E}\|$[110], as indicated in the figure. In order to assess the overall average relaxation over the total regions imaged in Figs. 1 and 2, we show, in Fig. 4, *spatially integrated* LPCL spectra over these same regions of the (111)*A* and (111)*B* misoriented samples. The electron beam was ras-

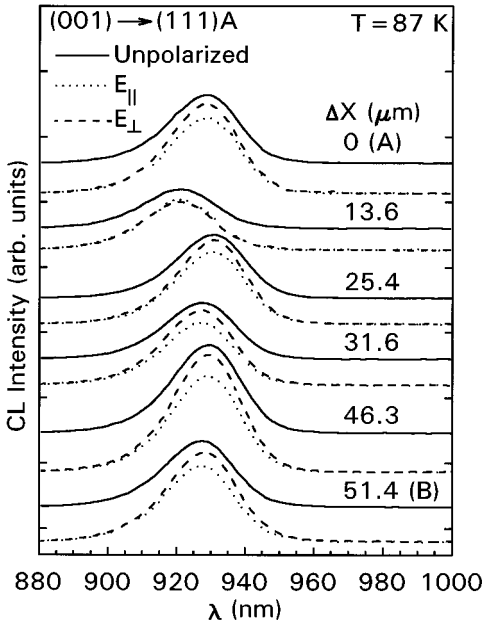

FIG. 3. Local CL (solid line) and LPCL spectra for the (111)*A*-misoriented sample along the dashed line indicated in Fig. 1(b). The distance, Δx, along the dashed line from the point *A* is indicated. The LPCL spectra were acquired under $\mathbf{E}_{\perp}$ (dashed line) and $\mathbf{E}_{\parallel}$ (dotted line) polarizer orientations, where the electric field vector subscripts denote perpendicular and parallel to [110], respectively.

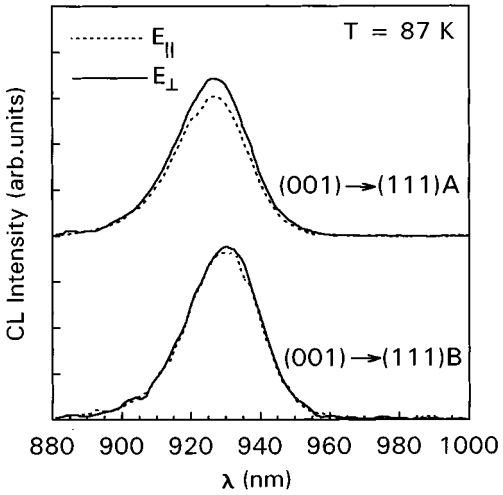

FIG. 4. Spatially averaged LPCL spectra over the (111)*A*- and (111)*B*-misoriented samples. The sampled regions correspond to the same 128×94 μm^2 regions shown in Figs. 1 and 2. $\mathbf{E}_{\perp}$ and $\mathbf{E}_{\parallel}$ refer to electric field vector **E** perpendicular and parallel to [110].

tered over a 128 μm$\times$94 μm region on each sample during acquisition. These spatially integrated spectra were taken with the polarizer rotated to detect emission of light with $\mathbf{E}\perp[110]$ and $\mathbf{E}\|[110]$ detection orientations, as indicated. It is evident from both spectra that the GaAs(001) substrate misoriented towards (111)*A* exhibits a greater degree of average polarization anisotropy as compared to the one misoriented towards (111)*B*. The values of $I_\parallel/I_\perp$ are 0.85 and 0.99 for the samples grown on the (111)*A*- and (111)*B*-misoriented substrates, respectively, where I is the integrated intensity and the subscript refers to its electric field orientation. The reduction of the polarization anisotropy for the (111)*B* misorientation reflects a change in the preferential direction for the initial relaxation which evidently depends on the substrate misorientation. The spatially integrated LPCL spectra for the (111)*B*-misoriented sample are shifted $\sim$5 nm towards longer wavelengths relative to the spectra for the (111)*A*-misoriented sample in Fig. 4, consistent with the greater average strain relaxation in the (111)*B* sample as measured in XRC.

Interband optical transitions involving the hh and lh states exhibit polarization selection rules which depend on the strain tensor, deformation potentials, and orientation of the electric field, **E**, of light emitted or absorbed.[10] For a [110]-oriented pure uniaxial compressive stress (i.e., $\sigma_\parallel=0$), very little mixing of the hh and lh bands occurs. The excitonic emission associated with the lh valence band is the lowest energy transition and is partially linearly polarized parallel to [110]. For the special case of small hh and lh mixing for a uniaxial compressive stress in $In_{0.13}Ga_{0.87}As$, the ratio of oscillator strengths of light with $\mathbf{E}\|[110]$ polarization to that with $\mathbf{E}\perp[110]$ is $\sim$1/4 (i.e., $I_\parallel/I_\perp\approx1/4$). For regions of pure biaxial stress involving $\sigma_\perp=\sigma_\parallel$, the hh excitonic transition has lowest energy and $I_\parallel/I_\perp=1$. Thus, LPCL can sensitively detect deviations from homogeneous biaxial stress.

For the current samples, the foregoing discussion suggests that the polarization anisotropies are consistent with quasi-uniaxial stresses along [110] and [110] for the (111)*A* and (111)*B* misoriented samples, respectively, with the (111)*A* having a larger average stress. The term quasi-uniaxial connotates $\sigma_\perp\neq\sigma_\parallel$ with the larger stress component defining the uniaxial direction. The reduction of the total polarization anisotropy for the (111)*B* misorientation (see Fig. 4) is also consistent with the reduction in the strain asymmetry measured in XRC.

C. Correlation of LPCL with CLWI

It is apparent from the images of Figs. 1 and 2 that the blue- and red-shifted regions correspond to regions of smaller and larger polarization anisotropies, respectively, for both these samples. The local LPCL spectra of Fig. 3 show an example of a CL spectrum (at $\Delta x=13.6$ μm) which shows a reduced polarization anisotropy associated with a blue-shift. Histograms along an arbitrary [110]-oriented line of Figs. 1 and 2 are shown in Figs. 5 and 6, respectively, revealing the spatial correlation between energy shift and polarization. The dashed and dotted vertical lines, respectively, illustrate the correlation between regions of enhanced red-shift with decreased $I_\parallel/I_\perp$ and enhanced blue-shift with

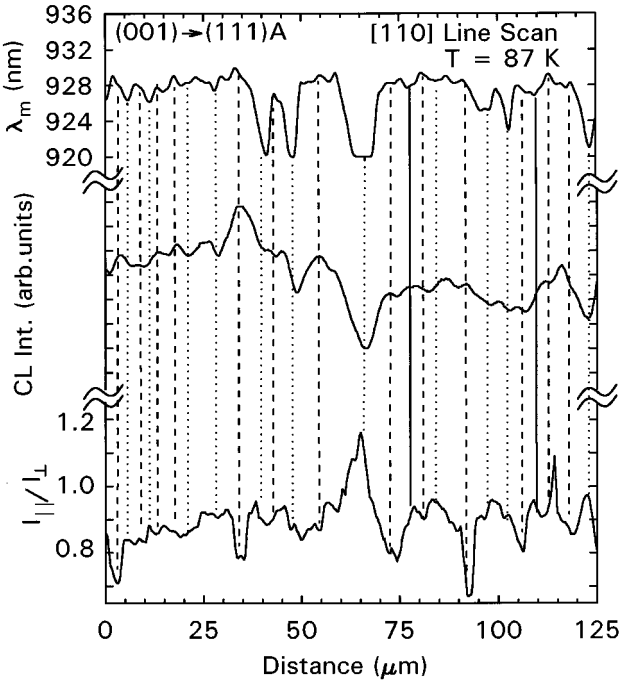

FIG. 5. Histograms of CLWI, integrated CL intensity and LPCL $I_\parallel/I_\perp$ ratio for an arbitrary line scan along [110] for the samples grown on the (111)*A*-misoriented substrate.

increased $I_\parallel/I_\perp$. The increase in polarization anisotropy ($I_\parallel/I_\perp<1$) indicates an enhancement in the quasi-uniaxial character of the stress which is largest for the red-shifted regions in both samples. The region of Fig. 1 shows a preferential DLD line direction along [110], while the region of Fig. 2 shows slightly greater DLD densities with a line di-

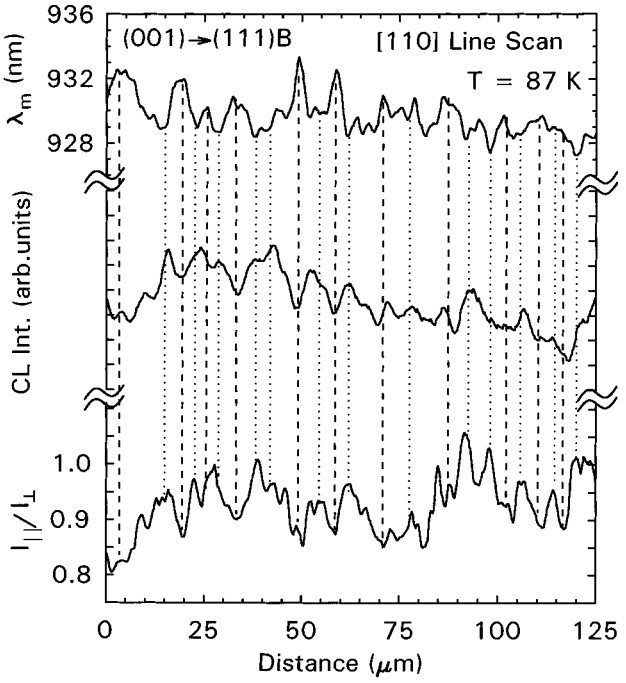

FIG. 6. Histograms of CLWI, integrated CL intensity and LPCL $I_\parallel/I_\perp$ ratio for an arbitrary line scan along [110] for the samples grown on the (111)*B*-misoriented substrate.

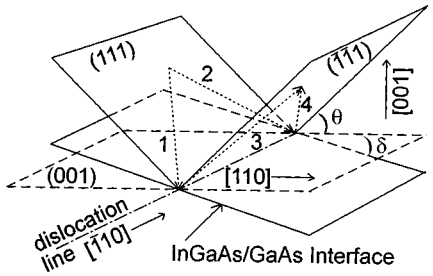

FIG. 7. View of {111} slip planes for a (001) substrate misoriented an angle δ towards (111)*A*. The geometry of the Burgers vectors, labeled 1–4, are shown for a [110]-oriented α dislocation.

rection along [110]. In Fig. 1, the red-shifted regions indicate regions of greater relaxation along [110], with misfit dislocations occurring preferentially along [110] (i.e., α dislocations). A particularly striking feature of the data for the (111)*A* misorientation is the reduction in luminescence efficiency (from the spectrally integrated CL data of Figs. 1 and 5) near regions of enhanced compressive stress (blue-shifted regions) for the (111)*A* misorientation. Regions of the blue-shift in Fig. 1 show a reduced luminescence efficiency despite a reduction in total strain relaxation. The converse, however, is true for the (111)*B* misorientation which shows an increase in luminescence efficiency near regions of blue-shift, as seen in Figs. 2 and 6. In both cases the relative blue-shifts reflect a greater average biaxial stress and correspond to a reduced polarization anisotropy. Some blue-shifted regions of Figs. 1 and 5 show a reversal in the polarization anisotropy where $I_{\parallel}/I_{\perp}>1$. This can only happen if the direction of quasi-uniaxial stress changes direction. It is possible that a large local decrease in the [110]-oriented α dislocations relative to the [110]-oriented β dislocations will induce a quasi-uniaxial stress along [110], despite having a greater average density of α dislocations throughout the sample.

D. Analysis of anisotropic strain relaxation

These features represent the complex nature of the strain relaxation and may relate to the differences in carrier recombination rates associated with α ([110] line direction) and β ([110] line direction) dislocation cores and point defects associated with these dislocations. These two types of 60° dislocations are chemically inequivalent, owing to the difference in termination of the extra half-plane which, e.g., in the type-I (shuffle) set has a Ga and As termination, respectively, for the unreconstructed α and β dislocation cores. For a nonvicinal GaAs(001) substrate (i.e., nominally no misorientation) it is well established that for single thin $In_xGa_{1-x}As$ ($x\leqslant 0.2$) films grown on GaAs(001), α dislocations are the first to form in relaxing the strain.[4,5] This has previously been attributed to the different levels of stress required to nucleate α and β dislocations and the differences in α and β dislocation propagation velocities on nonvicinal GaAs(001) substrates.[14,15]

The asymmetries found in the XRC and CL data can be understood by considering the influence of the GaAs(001) miscuts towards (111)*A* and (111)*B* on the stress experienced by the relevant {111} slip systems of 60° α and β dislocations. Consider the geometry of a [110] oriented dislocation, as shown in Fig. 7. The two possible {111} glide planes for this dislocation, (111) and $(\bar{1}11)$, intersect the (001) plane at an angle $\theta=54.7°$. The four possible Burgers vectors for this dislocation are $\frac{1}{2}[101]$, $\frac{1}{2}[011]$, $\frac{1}{2}[0\bar{1}1]$, and $\frac{1}{2}[\bar{1}01]$, and are labeled 1–4, respectively, in Fig. 7. The strain relaxation by a given misfit dislocation is in proportion to the magnitude of the Burgers vector component perpendicular to the dislocation projected onto the interface plane. For the positive miscut angle δ depicted in the figure, Burgers vectors 1 and 2 will have larger perpendicular components projected onto the interface compared to those for Burgers vectors 3 and 4. Therefore, Burgers vectors 1 and 2 will have a slightly greater driving force for interface formation than that of 3 and 4. The tilt component of Burgers vectors 1 and 2 is toward the interface, and this tendency for formation of a preferential Burgers vector set has previously been used to explain the direction of epilayer tilt in strained heterostructure systems with vicinal substrates.[16,17] For a (111)*A* misorientation angle δ ($\delta=2°$ in this study), the (111) and $(\bar{1}\bar{1}1)$ planes make angles of $\theta-\delta$ and $\theta+\delta$, respectively, with the $In_{0.13}Ga_{0.87}As$/GaAs interface. During the initial phase of $In_{0.13}Ga_{0.87}As$ growth, the film will be under a homogenous biaxial stress $\sigma_{\perp}=\sigma_{\parallel}=\sigma$. The differences in the strain relaxation between the two samples can now be explained by considering differences in the shear stress on {111} slip systems with substrate misorientation angle δ since the glide force per unit length is proportional to the shear stress. These differences in glide force caused by the misorientation will then be in competition with inherent differences in α and β dislocation formation energies which are already present in nonvicinal strained systems. For a (111)*A* miscut, as depicted in Fig. 7, the shear stress, τ_1, on the slip system for an α dislocation defined by the (111) glide plane and Burgers vector 1 ($\frac{1}{2}[101]$) is[18]

$$\tau_1=\frac{\sigma}{\sqrt{6}}\left(\cos^2\delta+\frac{1}{\sqrt{2}}\sin\ \delta\cos\ \delta-\sin^2\delta\right). \tag{1}$$

The formation of [110] oriented dislocations (β type) will involve glide on $(11\bar{1})$ and (111) planes. The relevant slip system for glide on (111) involves Burgers vector 2 ($\frac{1}{2}[011]$). The resulting shear stress, τ_2, on this slip system for the (111)*A* misorientation of Fig. 7 is

$$\tau_2=\frac{\sigma}{\sqrt{6}}\left(\cos^2\delta-\frac{1}{\sqrt{2}}\sin\ \delta\cos\ \delta\right). \tag{2}$$

For small δ, $\tau_1>\tau_2$, and the driving force for α dislocations is further enhanced for the (111)*A* miscut. This would explain the large anisotropic relaxation seen in XRC and CL imaging which indicates a greater density of α dislocations compared to β dislocations. For the miscut towards (111)*B*, the converse is true by the same arguments leading up to Eqs. (1) and (2), and the formation of β dislocations will now become more favorable due the enhanced stress on a (111)*B* slip plane. This greater shear stress will still be in competition with a reduced inherent α dislocation formation

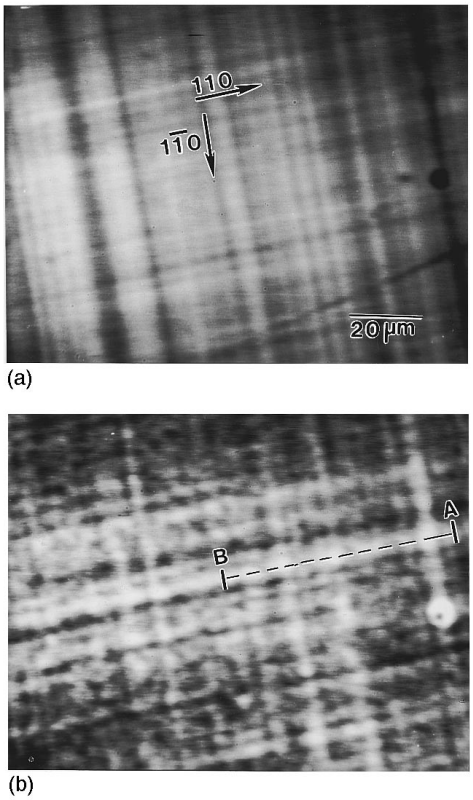

FIG. 8. Monochromatic CL images at (a) $\lambda = 929$ nm and (b) $\lambda = 1060$ nm showing a region containing long-wavelength emission for the (111)*A*-misoriented sample.

energy, which minimizes the resulting dislocation and strain relaxation anisotropy in the (111)*B* miscut orientation. Thus, the simple model qualitatively explains the anisotropic strain relaxation and concomitant excitonic polarization properties.

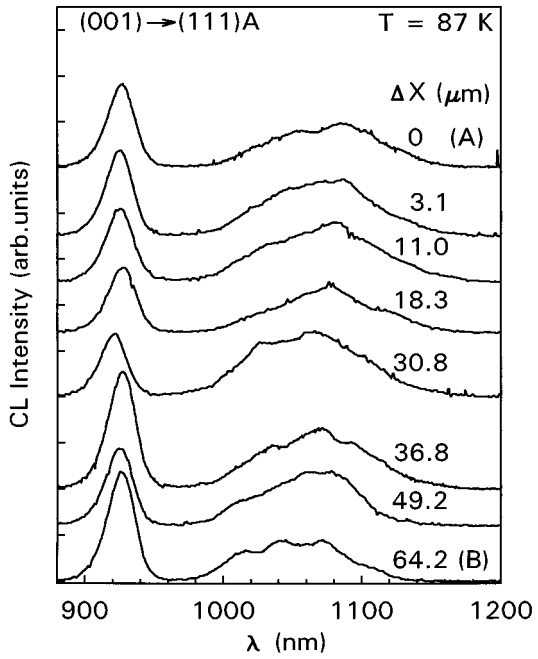

FIG. 9. Local CL spectra taken along the line *A*-*B* as shown in Fig. 8(b). The distance, Δx, along this line is shown.

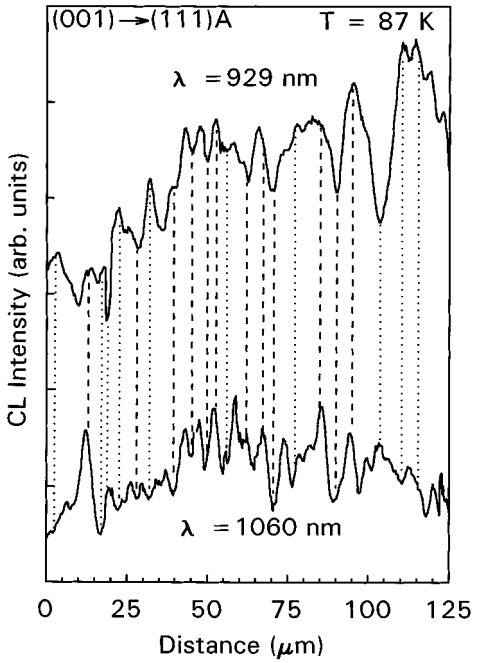

FIG. 10. Histograms of the CL imaging at $\lambda = 929$ nm and $\lambda = 1060$ nm along an arbitrary [110] oriented line.

E. Defect-induced long-wavelength emission

Some small isolated regions of the (111)*A*-misoriented sample were found to exhibit additional long-wavelength emission in the $1000 \lesssim \lambda \lesssim 1100$ nm range. Such emission was not found on the (111)*B* misoriented substrate. The region previously studied for (111)*A* in Fig. 1 also showed no detectable emission in the 1000 to 1100 nm range. Monochromatic CL images for $\lambda = 929$ nm and $\lambda = 1060$ nm are shown in Figs. 8(a) and 8(b), respectively, for a different region of the (111)*A*-misoriented sample. A stack plot of local CL spectra is shown in Fig. 9. The electron beam was positioned along the line shown in Fig. 8(b) and the position of each of the spectra relative to the starting point *A* are shown. The images showing DLDs in Figs. 8(a) and 8(b), appear similar. A histogram over a [110]-oriented line, as shown in Fig. 10, reveals that there is, for the most part, a correlation in the excitonic and long-wavelength peak intensities. That is, where excitonic emission is weak, a reduced long-wavelength emission is also observed. It is evident then that the reduction in the excitonic luminescence efficiency is due to carriers recombining by other recombination channels, both radiative at longer wavelengths and nonradiative in character. Previous studies have shown that an enhancement of the dislocation density can lead to long-wavelength emission.[11–13] The overall image contrast in Fig. 8(b) is determined by a competition of long-wavelength channels with nonradiative sources. The histograms of Fig. 10 show regions where peaks and dips in excitonic luminescence efficiency correspond with peaks and dips, respectively, in long-wavelength emission (dashed vertical lines). We observe some regions where there exists an anti-correlation between the occurrence of peaks and dips in the 929 and 1060 nm histograms (dotted vertical lines). Again, the complexity of

the strain relaxation may lead to regions of dislocations bunching and generation of point defects which have significant long-wavelength radiative recombination rates compared to the nonradiative recombination rate near dislocations which appears to dominate for recombination of excess carriers in most $In_xGa_{1-x}As/GaAs$ thin film systems that lead to DLDs.[11] Similarly, previous studies of defect-induced long-wavelength emissions in $In_{0.2}Ga_{0.8}As/GaAs$ multiple quantum wells showed that competing nonradiative channels lead to spatially correlated DLDs at both the quantum well e-hh excitonic transition energy and the subgap emissions.[11]

IV. CONCLUSION

We have studied the optical and structural properties of $In_{0.13}Ga_{0.87}As$ films grown on GaAs(001) misoriented 2° towards (111)*A* and (111)*B* planes. Spectrally integrated CL, monochromatic CL, LPCL, and CLWI imaging were used to study the spatial variations of the optical properties. For the (111)*A* misorientation, the XRC and CL measurements indicated that the density of [110]-oriented (α) dislocations was found to be greater than [110]-oriented (β) dislocations, giving rise to a net polarization anisotropy. The polarization anisotropy was reduced for the growth on the (111)*B*-misoriented sample, consistent with XRC measurements. A model discussing the changes in stress on ⟨110⟩{111} slip systems caused by the substrate offcut explains the change in relaxation asymmetry between the (111)*B* and (111)*A* misorientations. The large dislocation density ($>10^5$ cm^{-1}) was found to lead to DLDs comprised of bunches of dislocations, forming blue- and red-shifted bands observed in the CLWI imaging. Isolated regions of the (111)*A* sample showed regions of defect-induced long-wavelength emission. These results show that the polarization and relaxation anisotropy of $In_xGa_{1-x}As$ can be tailored with a suitable choice of the misorientation for the starting GaAs(001) substrate.

ACKNOWLEDGMENTS

This work was supported by the Charles Lee Powell Foundation, NSF(PYI-DMR), NSF(RIA-ECS), the Office of Naval Research, and the Army Research Office.

[1]R.S. Goldman, H.H. Wieder, K.L. Kavanagh, K. Rammohan, and D.H. Rich, Appl. Phys. Lett. **65**, 1424 (1994).
[2]Z. Liliental-Weber, Y. Chen, P. Werner, N. Zakharov, W. Swider, and J. Washburn, J. Vac. Sci. Technol. B **11**, 1379 (1993).
[3]K. Rammohan, Y. Tang, D.H. Rich, R.S. Goldman, H.H. Wieder, and K.L. Kavanagh, Phys. Rev. B **51**, 5033 (1995).
[4]K.L. Kavanagh *et al.*, J. Appl. Phys. **64**, 4843 (1988).
[5]E.A. Fitzgerald, G.P. Watson, R.E. Proano, D.G. Ast, P.D. Kirchner, G.D. Pettit, and J.M. Woodall, J. Appl. Phys. **65**, 2220 (1989).
[6]K. Rammohan, D.H. Rich, R.S. Goldman, J. Chen, H.H. Wieder, and K.L. Kavanagh, Appl. Phys. Lett. **66**, 869 (1995).
[7]D.H. Rich *et al.*, Phys. Rev. B **43**, 6836 (1991).
[8]Y. Tang, D.H. Rich, E.H. Lingunis, N.M. Haegel, J. Appl. Phys. **76**, 3032 (1994).
[9]M. Grundmann, J. Christen, D. Bimberg, A. Hashimoto, T. Fukunaga, and N. Watanabe, Appl. Phys. Lett. **58**, 2090 (1991).
[10]F.H. Pollak and M. Cardona, Phys. Rev. **172**, 816 (1968).
[11]D.H. Rich, T. George, W.T. Pike, J. Maserjian, F.J. Grunthaner, and A. Larsson, J. Appl. Phys. **72**, 5834 (1992).
[12]M.J. Joyce, M. Gal, and J. Tann, J. Appl. Phys. **65**, 1377 (1989).
[13]D.H. Rich, K.C. Rajkumar, Li Chen, A. Madhukar, and F.J. Grunthaner, Appl. Phys. Lett. **61**, 222 (1992).
[14]T. George, E.R. Weber, S. Nozaki, T. Yamada, M. Konagai, and K. Takahashi, Appl. Phys. Lett. **59**, 60 (1991).
[15]I. Yonenaga and K. Sumino, J. Appl. Phys. **65**, 85 (1989).
[16]K.L. Kavanagh, R.S. Goldman, and J.C.P. Chang, Scan. Microsc. (in press).
[17]J.E. Ayers, S.K. Ghandhi, and L.J. Schowalter, J. Cryst. Growth **113**, 430 (1991).
[18]For a calculation of stress on ⟨110⟩{111} slip systems see, e.g., J.P. Hirth and J. Lothe, *Theory of Dislocations*, 2nd ed. (Krieger, Malabar, FL, 1992), Chap. 9.